Functional α6β4 acetylcholine receptor expression enables pharmacological testing of nicotinic agonists with analgesic properties

Daniel Knowland, Shenyan Gu, William A. Eckert III, G. Brent Dawe, Jose A. Matta, James Limberis, Alan D. Wickenden, Anindya Bhattacharya, and David S. Bredt

Neuroscience Discovery, Janssen Pharmaceutical Companies of Johnson & Johnson, San Diego, California, USA.

The α6β4 nicotinic acetylcholine receptor (nAChR) is enriched in dorsal root ganglia neurons and is an attractive non-opioid therapeutic target for pain. However, difficulty expressing human α6β4 receptors in recombinant systems has precluded drug discovery. Here, genome-wide screening identified accessory proteins that enable reconstitution of human α6β4 nAChRs. BARP, an auxiliary subunit of voltage-dependent calcium channels, promoted α6β4 surface expression while IRE1α, an unfolded protein response sensor, enhanced α6β4 receptor assembly. Effects on α6β4 involve BARP's N-terminal region and IRE1α's splicing of *XBP1* mRNA. Furthermore, clinical efficacy of nicotinic agents in relieving neuropathic pain best correlated with their activity on α6β4. Finally, BARP-knockout, but not NACHO-knockout mice lacked nicotine-induced antiallodynia, highlighting the functional importance of α6β4 in pain. These results identify roles for IRE1α and BARP in neurotransmitter receptor assembly and unlock drug discovery for the previously elusive α6β4 receptor.

Introduction

Chronic pain is a serious unmet public health issue in need of non-opioid analgesics. Epibatidine has long been recognized as a potent analgesic through actions on nicotinic acetylcholine receptors (nAChRs), yet negative side effects preclude its clinical use. nAChRs transduce synaptic signals and mediate diverse physiological actions of ACh in the brain and periphery (1–6). nAChRs comprise a large family of homo- and heteropentamers assembled from 10 α (α1–α10, α8 only found in chick) and 4 β (β1–β4) subunits, each with discrete expression patterns. The α4β2 receptor is thought to be the subtype mediating nAChR-induced analgesia; however, despite significant investment there are no approved nicotinic agents for analgesia, suggesting that a different subtype may be involved (7).

Recently, animal and human studies have implicated dorsal root ganglia–enriched (DRG-enriched) α6β4 receptors in chronic pain states. Phenotypic analysis of inbred mice found that α6 levels in DRGs vary inversely with injury-induced allodynia, and loss-of-function variants in the α6 promoter region correlate with chronic postoperative pain (8). Furthermore, α6-knockout (α6-KO) mice suffer increased allodynia, whereas α6 gain-of-function models show attenuated pain levels (8). Collectively, α6-containing receptors in the DRG represent an attractive non-opioid approach for the treatment of pain.

Although nAChRs are appealing therapeutic targets, drug discovery and basic science efforts are hampered because most subtypes are not expressed as functional proteins in cell lines. Especially problematic are human α6–containing receptors, which do not form functional channels in any recombinant expression system (9, 10). We previously identified NACHO, an endoplasmic reticulum (ER) protein, which serves as a client-specific chaperone that promotes function of many nAChRs and is essential for assembly of α7 homopentamers (11, 12). NACHO also mediates assembly of dopamine neuron–enriched α6β2β3 receptors, which also require additional protein accessories including β-anchoring and -regulatory protein (BARP), SULT2B1, and LAMP5 (13). Whether DRG-enriched α6β4 shows similar dependency on NACHO and other accessory components for functional expression is unknown.

To assess this, we performed genome-wide cDNA screening for proteins that enable robust functional expression of human α6β4 receptors. Our screen identified BARP and inositol-requiring enzyme-1α (IRE1α) as α6β4 enhancers. BARP is a single-pass transmembrane protein that was first identified in association with voltage-gated calcium channel β subunits (14) and was later found as an accessory component of α6β2β3 nAChRs (13), while IRE1α is a constituent of the unfolded protein response (UPR) (15). We found that the efficacy of nicotinic agonists to treat neuropathic pain best correlates with their activity on α6β4 receptors. Furthermore, *BARP*-KO mice, which show diminished α6β4 surface expression in DRG, have blunted antiallodynic responses to nicotine and ABT-594, a clinically effective nicotinic agent, suggesting that α6β4 activity is critical for neuropathic pain relief.
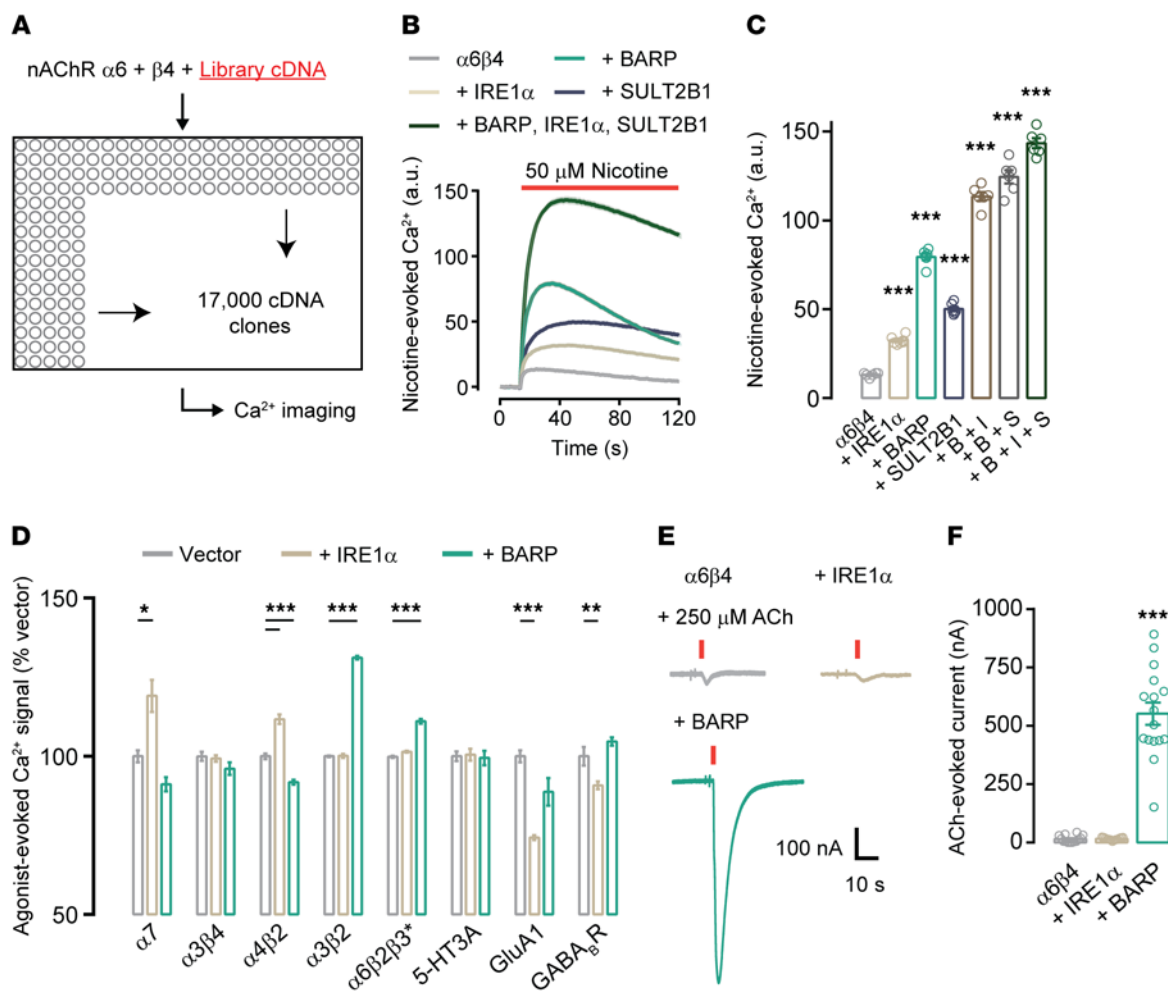
Figure 1. Genomic screening identifies chaperones for functional α6β4 reconstitution. (**A**) Schematic of genomic screening. HEK293T cells were cotransfected with cDNAs encoding α6 and β4 and individual plasmids from a genome-wide expression library. Ca²⁺ signals were measured in a fluorescence imaging plate reader (FLIPR). (**B**) Exemplary FLIPR traces showing nicotine-induced Ca²⁺ responses for indicated transfections. (**C**) Quantification of FLIPR signals. Activity of α6β4 is enhanced by BARP, IRE1α, and SULT2B1. $n = 6$ for each group. B, BARP; I, IRE1α; S, SULT2B1. (**D**) Quantification of FLIPR Ca²⁺ response from other nAChRs and other ion channels (5-HT3A and GluA1), and G protein–coupled receptor (GABA$_B$R) cotransfected with either BARP or IRE1α. nAChRs were stimulated with 50 μM nicotine, 5-HT3A with 100 μM serotonin, GluA1 with 100 μM glutamate plus 100 μM cyclothiazide, and GABA$_B$R with 100 μM GABA. $n = 6$ each. Responses normalized to that of vector-transfected cells (100%). (**E**) Current traces from *Xenopus* oocytes injected with indicated cRNAs and stimulated with a 2-second pulse of 250 μM ACh. (**F**) Quantification of current amplitude (absolute value) responses in **E**: $n = 14$, 13, and 16 oocytes for α6β4, α6b4 plus IRE1α, and α6β4 plus BARP, respectively. *$P < 0.05$, **$P < 0.01$, ***$P < 0.001$ by 1-way ANOVA with Dunnett's post hoc correction for multiple comparisons to vector (**C**, **D**, and **F**). **C**: $F_{6,35} = 511.4$. **D**: α7, $F_{2,15} = 18.08$; α4β2, $F_{2,15} = 86.27$; α3β2, $F_{2,15} = 1171$; α6β2β3*, $F_{2,15} = 143.9$; GluA1, $F_{2,15} = 21.46$; GABA$_B$R, $F_{2,15} = 12.85$. **F**: $F_{2,40} = 106.7$. Graphs are the mean ± SEM and depict 1 experiment that was replicated with similar results.

Results

Genome-wide screening identifies BARP and IRE1α as α6β4 accessory proteins. To identify functional regulators of α6β4, we cotransfected HEK293T cells with cDNAs encoding α6 and β4 along with individual clones from a library of approximately 17,000 plasmids that express nearly all predicted human proteins. Using a fluorescence imaging plate reader (FLIPR) to measure nicotine-evoked Ca²⁺ responses, we identified 2 clones that augmented responses from α6β4 (Figure 1, A–C). The clone that most robustly enhanced the FLIPR signal was BARP, which we previously identified as an auxiliary subunit of α6β2β3 receptors (11). In those previous studies, we found that SULT2B1, LAMP5, and NACHO are also accessories for α6β2β3 (13). Here, we found that SULT2B1, but not NACHO or LAMP5, also augmented nicotine-evoked responses

from α6β4 (Figure 1, B and C; Supplemental Figure 1A; supplemental material available online with this article; https://doi.org/10.1172/JCI140311DS1).

The second-best enhancer of α6β4 activity identified from the screen was IRE1α of the UPR (15) (Figures 1, B and C). By contrast, 2 other UPR components, PERK and ATF6 (16), did not affect α6β4 FLIPR responses (Supplemental Figure 1A). We confirmed that these nicotine-evoked Ca²⁺ signals were mediated by α6, as α-conotoxin MII, an α6-selective antagonist (17), completely blocked responses from α6β4, but not those from α4β2 or α3β4 (Supplemental Figure 1, B and C).

We next asked whether BARP and IRE1α could also enhance responses from other nAChR subtypes. BARP promoted function of α6β2β3* (where * indicates the use of the β3 mutant sub-

unit [V273S]) and α3β2 but had no effects on the other nAChRs tested (Figure 1D). Interestingly, IRE1α enhanced α7, α4β2, and α6β2β3* to modest degrees (Figure 1D). Neither BARP nor IRE1α increased responses from other ligand-gated ion channels including 5-HT3A or GluA1, or the class C GPCR GABA_BR (Figure 1D).

We next explored the effects of BARP and IRE1α using 2-electrode voltage clamp in *Xenopus* oocytes. Previous studies have been unable to produce large, reliable human α6β4 currents in oocytes and instead have relied on chimeric or rodent receptors (9, 17–19). Similarly, we detected minimal to no ACh-evoked currents following oocyte injection with α6 and β4 cRNAs (14.91 ± 4.016 nA). Strikingly, coinjection with BARP cRNA consistently enabled large ACh-evoked currents (551.9 ± 47.39 nA; Figure 1, E and F). By contrast, IRE1α cRNA had no effect (15.78 ± 1.549 nA; Figure 1, E and F). In whole-cell patch clamp electrophysiology on HEK293T cells transfected with α6β4 alone, small and inconsistent ACh-evoked (1 mM) currents were evoked (107.27 ± 44.96 pA). However, similarly to oocytes, HEK293T cells coexpressing BARP with α6β4 produced larger, reliable currents (566.06 ± 226.02 pA), whereas those coexpressing IRE1α did not (20.30 ± 10.43 pA; Supplemental Figure 1, D and E). In HEK293T cells, BARP enhanced the peak amplitude of ACh-evoked currents from α6β4 but did not alter channel gating properties, as the steady-state–to–peak current ratio was the same in the absence or presence of BARP (Supplemental Figure 1F).

BARP and IRE1α enable α6β4 functional expression through different mechanisms. We next explored cellular mechanisms underlying the effects of BARP and IRE1α on α6β4. To assess α6β4 surface expression, we used a β4 subunit containing a C-terminal, extracellular HA tag that does not interfere with receptor function (12). Cotransfection with BARP in HEK293T cells robustly enhanced α6β4 surface expression, whereas IRE1α did not (Figure 2, A and B). This BARP effect was specific, as BARP did not enhance α3β4 surface expression (Figure 2, A and B). We additionally tagged α6 with an extracellular V5 epitope and again found that BARP, but not IRE1α, enhanced surface expression (Supplemental Figure 2, A and B). In alignment with functional data (Supplemental Figure 1A), we found that the α6β2β3 accessory protein SULT2B1 enhanced α6β4 surface expression, while NACHO and LAMP5 did not (Supplemental Figure 2, A and B).

BARP is a single-pass transmembrane protein with cytosolic motifs that bind voltage-gated calcium-channel (VGCC) β subunits and negatively influences channel function (14). To determine whether BARP's effects on α6β4 and VGCCs share a common essential domain, we created a series of BARP mutants. BARP202, a truncated version lacking its VGCC β subunit–binding domain, retained α6β4 functionality for both FLIPR and surface expression (Supplemental Figure 3). Further truncation of BARP's intracellular region (BARP101) or deletion of BARP's transmembrane region (BARPΔTM) disrupted effects on α6β4 (Supplemental Figure 3). These experiments indicate that distinct domains are required for BARP's effects on α6β4 and VGCCs.

As IRE1α did not enhance α6β4 surface expression, we assessed effects on receptor assembly. Orthosteric ligands such as [³H]epibatidine interact at the interface of assembled nAChR subunits, and their binding quantifies receptor oligomerization (20). We

found that IRE1α, but not BARP, increased [³H]epibatidine binding to cotransfected α6β4 (Figure 2C); however, neither BARP nor IRE1α affected total α6 protein levels (Supplemental Figure 2C).

To assess protein interactions, we immunoprecipitated solubilized membranes from HEK293T cells cotransfected with α6 and β4 along with accessory proteins. As expected, immunoprecipitation of V5-tagged α6 revealed association with β4 (Figure 2D). We also observed an interaction with BARP and α6β4, indicating that BARP directly binds to α6β4. However, we observed no interaction with IRE1α (Figure 2D). We confirmed the specificity of the immunoprecipitation, as BARP was absent from immunoprecipitation when cotransfected with only β4 (Figure 2D, second lane). Taken together, our results demonstrate 2 separate roles for BARP and IRE1α that work to augment α6β4: IRE1α enhances receptor assembly, while BARP promotes trafficking to the membrane by directly binding to α6β4.

BARP acts on the transmembrane and cytosolic regions of α6. We next investigated which regions of α6 are required for BARP effects. Because BARP regulates α6β4 but not α4β4, we constructed α6/α4 receptor chimeras for cotransfection with β4 (Figure 3A). BARP was inactive on a chimera containing the extracellular N-terminal region of α6 fused to the α4 transmembrane and intracellular regions (α6N/4; Figure 3, B–D). Conversely, BARP robustly enhanced surface expression and FLIPR responses of the α4N/6 chimera (Figure 3, B–D). We further confirmed functionality in oocytes and again found that BARP enhanced ACh-evoked currents from α4N/6, but not from α6N/4 chimeras (Supplemental Figure 4, A and B). Taken together, these results show that the N-terminal extracellular domain of α6 is expendable for BARP-mediated effects, and that BARP directly interacts with α6β4 via its transmembrane regions.

RNase activity of IRE1α is necessary and sufficient for α6β4 assembly. Because IRE1α does not physically associate with α6β4, we wondered whether downstream signaling might be involved. Accumulation of unfolded proteins in the ER causes IRE1α to dimerize and *trans*-autophosphorylate its kinase domain, which thereby activates its RNase domain to splice the transcription factor *XBP1* to a unique protein, XBP1s (16). Accordingly, we generated IRE1α mutants (Figure 4A) that abolish kinase (K599A, KINmut) or RNase (K907A, RNAmut) activities (21), as reflected by reduced XBP1s production (Figure 4B). Next, we cotransfected each mutant with BARP and measured FLIPR responses. Compared with WT IRE1α, both mutants reduced upregulation of nicotine-evoked Ca²⁺ responses from α6β4 (Figure 4C). Additionally, STF-083010, an IRE1α RNase inhibitor (22), blocked IRE1α-mediated enhancement of α6β4 function but had no effect on α3β4 (Supplemental Figure 5, B–D). In line with IRE1α's role in α6β4 assembly, IRE1α KINmut and RNAmut reduced IRE1α-mediated enhancement of [³H]epibatidine binding (Figure 4D).

To isolate the contribution of IRE1α's RNase activity, we used a strategy developed by others (23) that combines an IRE1α kinase-dead mutant (I642G, CONDmut) with a drug (1NM-PP1) that binds to the mutated kinase domain and initiates IRE1α RNase activity independently of kinase activity (Figure 4A). Indeed, CONDmut showed reduced XBP1s, which was rescued with 1NM-PP1 (Figure 4B). In cells cotransfected with α6β4 and BARP, CONDmut IRE1α reduced the nicotine-evoked FLIPR
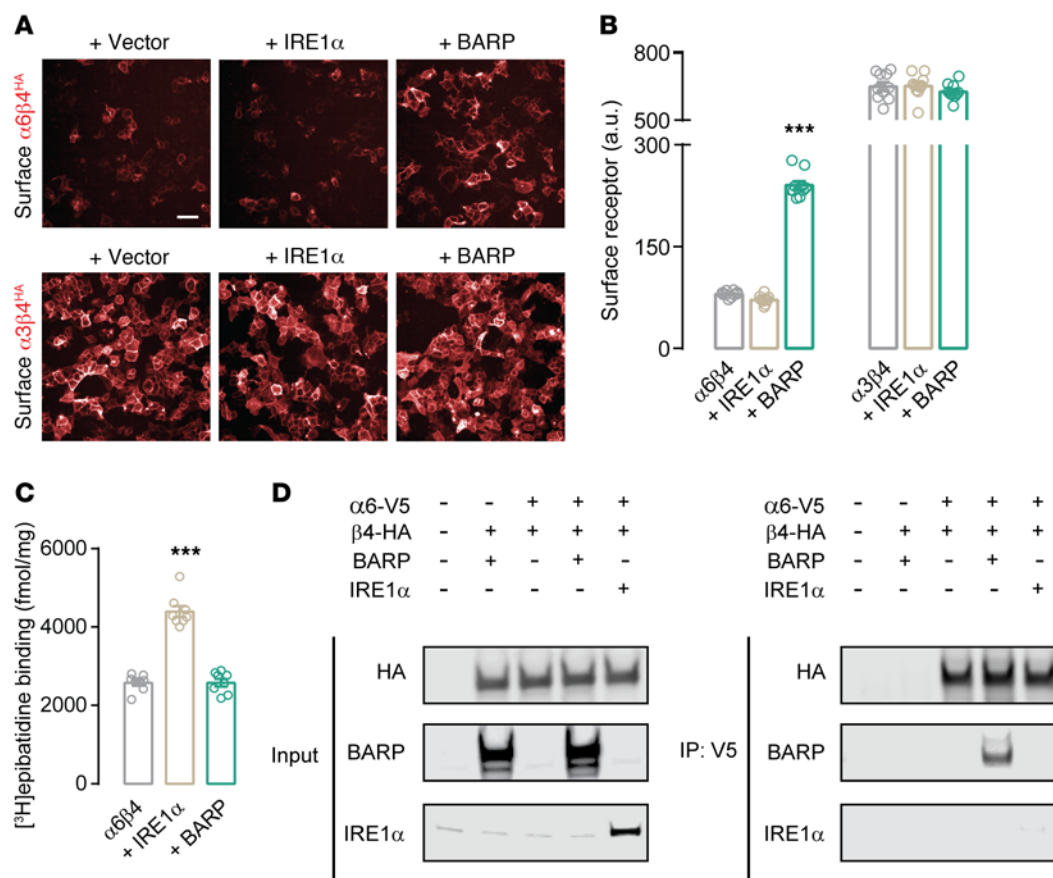
Figure 2. BARP and IRE1α promote α6β4 function through distinct mechanisms. (**A**) Confocal images of α6β4 and α3β4 surface staining in transfected HEK293T cells. The β4 subunit C-terminus contained an HA tag, which was visualized with an anti-HA antibody. (**B**) Quantification shows that BARP, but not IRE1α, enhances α6β4 surface staining. Neither has effects on α3β4. $n = 10$ for each group. Scale bar: 50 μm. (**C**) Quantification of [³H]epibatidine binding to HEK293T lysates transfected as indicated. $n = 8$ for each condition. (**D**) Immunoprecipitation with anti-V5 of solubilized HEK293T cells transfected as indicated. Immunoblotting shows that V5-tagged α6 associates with β4 and BARP, but not with IRE1α. ***$P < 0.001$ by 1-way ANOVA with Dunnett's post hoc correction for multiple comparisons to vector (**B** and **C**). **B**: $F_{3,36} = 515.9$. **C**: $F_{3,28} = 106.7$. Graphs are the mean ± SEM and depict 1 experiment that was replicated with similar results.

signal, which was restored with 1NM-PP1 (Figure 4E). Similarly, IRE1α CONDmut reduced [³H]epibatidine binding to HEK293T cells transfected with α6β4 and this binding was also restored with 1NM-PP1 (Figure 4F). We next asked whether XBP1s itself can augment α6β4 (Supplemental Figure 5A). Indeed, transfection of XBP1s enhanced α6β4 assembly and function (Figure 4, G and H). Collectively, these experiments suggest that IRE1α RNase activity targeting *XBP1* is critical for α6β4 assembly.

Endogenous IRE1α enhances α6β4 assembly. To assess whether activation of endogenous IRE1α promotes α6β4 assembly, we used tunicamycin (Tm), which inhibits N-linked glycosylation, and thereby induces ER stress and stimulates the UPR (24, 25). Previous reports showed that Tm-induced IRE1α activation peaks 4–8 hours after treatment and reduces back to baseline by 24 hours (25). Similarly, we found that 100 ng/mL Tm treatment for 4, but not 12 or 24 hours stimulated IRE1α activity to increase XBP1s (Figure 5A). Furthermore, 100 ng/mL Tm treatment for 4, but not 12 or 24 hours enhanced α6β4 FLIPR responses (Figure 5, B and C) and [³H]epibatidine binding (Figure 5D) in α6β4-plus-BARP cotransfections.

To explore effects of IRE1α activation on nAChRs in neurons, we first transduced cerebrocortical cultures with lentivi-

ruses expressing α6 and β4 subunits. Similarly to HEK293T cells, 4-hour, but not 24-hour, Tm treatment enhanced [³H]epibatidine binding (Figure 5E) and increased nicotine-evoked Ca²⁺ influx through α6β4 in neurons (Figure 5F). Furthermore, the IRE1α RNase inhibitor STF-083010 blocked the Tm-induced increase in [³H]epibatidine binding (Figure 5E). Also, Tm significantly enhanced nicotine-induced Ca²⁺ responses in untransduced cortical neurons (Figure 5G), which express endogenous α4β2 receptors that are also regulated by IRE1α (Figure 1D).

To confirm that Tm effects on α6β4 assembly specifically involve IRE1α activation, we used CRISPR/Cas9 to disrupt IRE1α in HEK293T cells. Immunoblotting demonstrated reduced or absent IRE1α in IRE1α-heterozygous (*IRE1α*-HET) and *IRE1α*-KO cell lines, respectively (Figure 5H). We also observed the expected reductions in Tm-induced XBP1s production in the *IRE1α*-HET and *IRE1α*-KO lines (Figure 5H).

Interestingly, *IRE1α*-KO cells showed reduced nicotine-evoked α6β4-mediated FLIPR responses (Figure 5I). By contrast, α3β4 and 5HT3A responses increased in *IRE1α*-KO cells (Supplemental Figure 6). In line with FLIPR data, *IRE1α*-KO cells also exhibited reduced [³H]epibatidine binding (Figure 5J). As expected, 4-hour
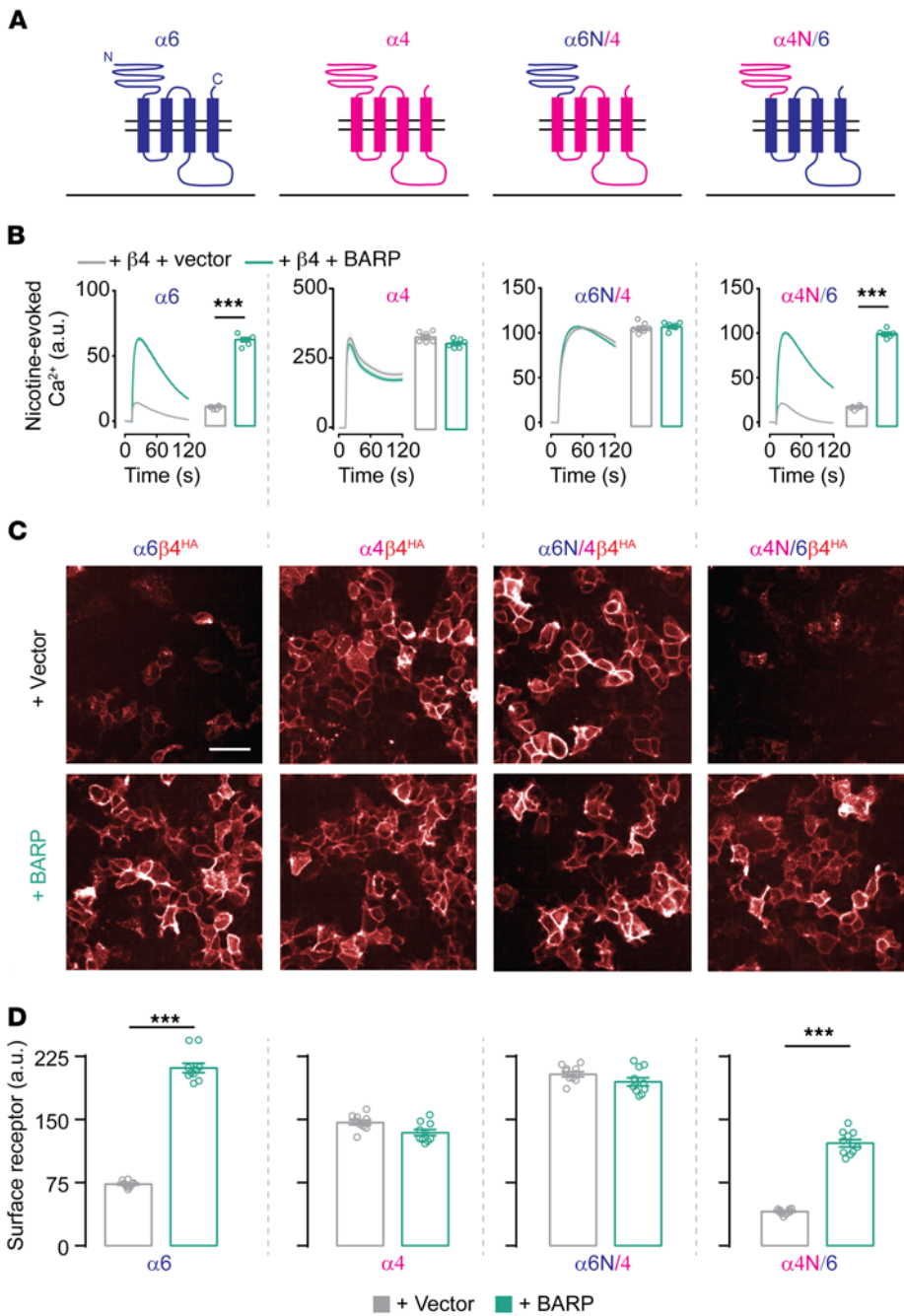
Figure 3. Transmembrane, but not N-terminal region, of α6 is critical for BARP effect. (A) Schematics of α6/α4 chimeras. **(B)** FLIPR traces and quantification of nicotine-evoked (50 μM) Ca²⁺ responses. *n* = 6 for each group. BARP enhances FLIPR responses only in α6- and α4N/6-containing receptors cotransfected with β4. **(C)** Representative confocal images for β4ᴴᴬ surface staining in cotransfected HEK293T cells with (bottom) and without (top) BARP. Scale bar: 50 μm. **(D)** Quantification of surface receptor intensity in **C**. *n* = 10 for each group. All chimeric α6/α4 nAChRs were cotransfected with β4 into HEK293T cells. ***P < 0.0001 by unpaired *t* test (**B** and **D**). **B**: α6β4, *t* = 29.95; α4N/6, *t* = 40.58. **D**: α6β4, *t* = 24.04; α4N/6, *t* = 18.19. Graphs are the mean ± SEM and depict 1 experiment that was replicated with similar results.

BARP regulates sensory neuron α6β4 and nicotine-induced antiallodynia. α6 and β4 Subunit mRNAs are selectively coexpressed in DRG (Supplemental Figure 7A) (26). In addition, α6β4-mediated currents have been recorded in DRG neurons and α6β4 receptors there modulate pain responses (8, 27). Here, we detected a BARP-immunoreactive band in DRG and cerebral cortical protein extracts that comigrated with BARP from transfected HEK293T cells but was absent from *BARP*-KO tissues (Figure 6A). Because there are no suitable antibodies to detect endogenous α6 or β4 (28), we transduced isolated DRG neurons with V5-tagged α6 and β4 from WT and *BARP*-KO mice. Compared with WT neurons, *BARP*-KO neurons had reduced α6β4 surface expression but equivalent total α6 (Figure 6, B and C), showing that BARP promotes α6β4 surface expression in neurons. In contrast, *BARP*-KO mice showed no difference from WT in α4β2 or endogenous α7 surface expression (Supplemental Figure 7, B–E).

The nicotinic agonist ABT-594, which is closely related to epibatidine, effectively treated diabetic neuropathic pain in clinical trials, but its development was discontinued due to side effects (29). A follow-up compound, ABT-894, developed to circumvent the nicotinic side effects, was not efficacious (30). The lack of efficacy for ABT-894 was hypothesized to reflect its increased specificity for α4β2 receptor, suggesting that other nAChRs underlie ABT-594's efficacy in neuropathic pain (30).

We wondered whether differential effects of ABT-894 and ABT-594 on α6β4 receptors could explain their contrasting clinical efficacies. We found that ABT-594, nicotine, and epibatidine — all of which have analgesic effects — exhibited similar agonistic efficacies on α4β2 and α6β4 receptors (Figure 6, D and E; Supplemental Tables 1 and 2). In contrast, ABT-894 was only weakly efficacious at α6β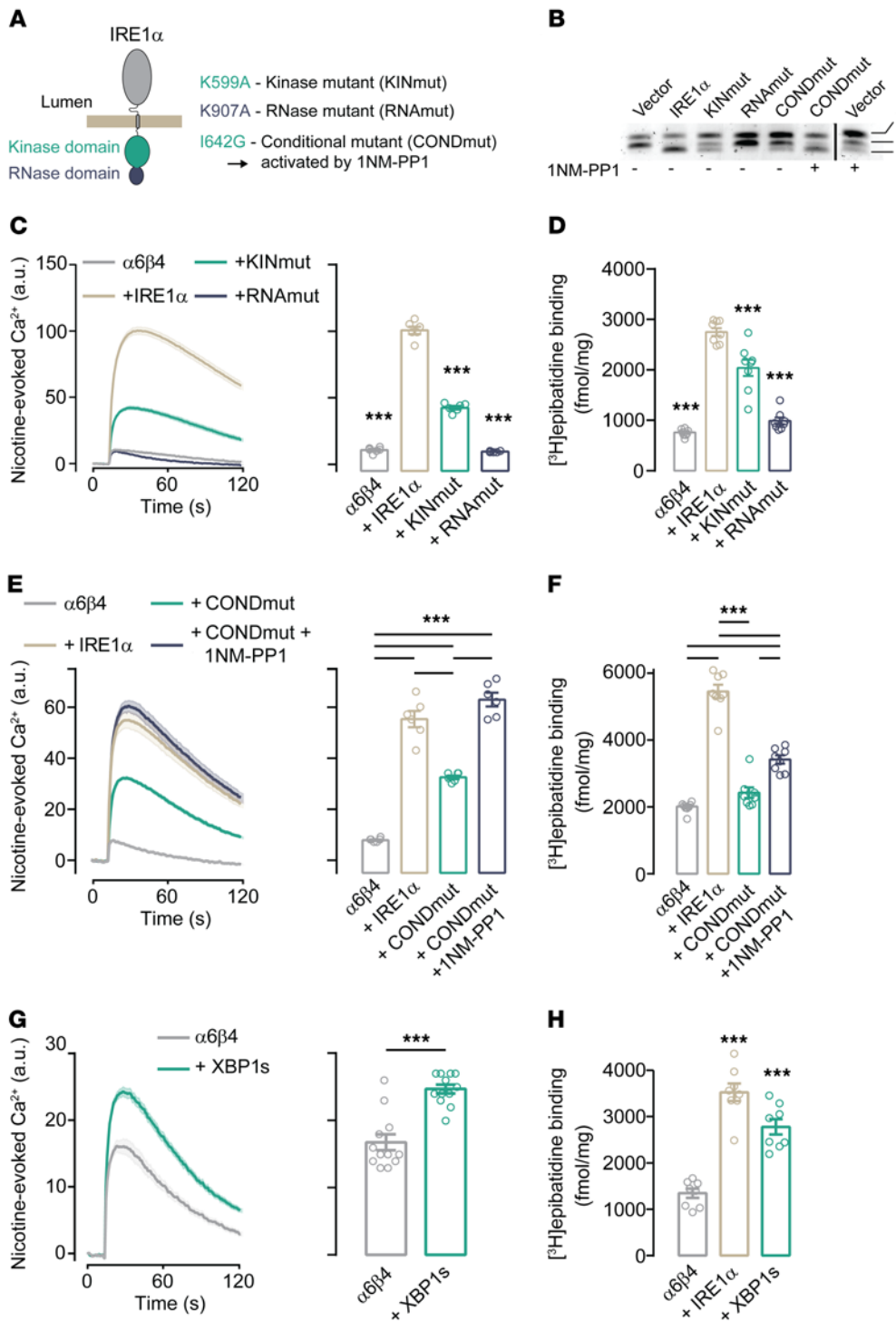4 as compared with α4β2 (Figure 6, D and E). All compounds tested behaved as full agonists at α3β4. Together, these compounds' activities on α6β4 may provide an explanation for the clinical failure of ABT-894 in diabetic neuropathic pain.

To explore α6β4's role in neuropathic pain in vivo, we evaluated *BARP*-KO animals in the spared nerve injury (SNI) model of neuropathic allodynia (31). No difference in mechanical allodynia

Tm application increased [³H]epibatidine binding to levels comparable to transfected IRE1α in WT cells (Figure 5K). In contrast, Tm failed to increase α6β4 [³H]epibatidine binding in *IRE1α*-KO cells but could be rescued when transfected with exogenous IRE1α (Figure 5K). These data demonstrate that endogenous IRE1α activity supports α6β4 assembly and function.

Figure 4. IRE1α RNase activity and XBP1 splicing mediate assembly of α6β4. (**A**) Schematics of IRE1α kinase domain (K599A, KINmut), RNase domain (K907A, RNAmut), and conditional (I642G, CONDmut) mutants that were transfected into HEK293T cells. (**B**) RT-PCR shows that IRE1α mutants decrease XBP1 splicing (lower band) as compared with WT IRE1α. 1NM-PP1 rescues XBP1s in I642G CONDmut. u = full-length unspliced XBP1, s = spliced XBP1 (XBP1s), * = hybrid amplicon. (**C**) FLIPR traces (left) and quantification (right) of HEK293T cells transfected with WT IRE1α, K599A mutant, or K907A mutant. IRE1α and mutants were cotransfected with BARP. n = 6 for each group. (**D**) IRE1α mutants reduce [³H]epibatidine binding in HEK293T cell lysates compared with WT IRE1α. n = 8 for each condition. (**E**) FLIPR traces (left) and quantification (right) of I642G CONDmut without and with 5 μM 1NM-PP1, which rescued the FLIPR response. (**F**) CONDmut reduces [³H]epibatidine binding. RNase activation of CONDmut with 5 μM 1NM-PP1 increases α6β4 assembly. n = 8 for each condition. (**G** and **H**) FLIPR traces (**G**, left), quantification (**G**, right), and [³H]epibatidine binding (**H**) from HEK293T cells cotransfected with α6β4 and XBP1s as indicated. n = 12 for each condition in **G**, n = 8 for each group in **H**. ***P < 0.001 by 1-way ANOVA with Dunnett's post hoc test to correct for multiple comparisons to WT IRE1α (**C** and **D**), 1-way ANOVA with Tukey's multiple-comparisons post hoc test (**E** and **F**), unpaired t test (**G**), or 1-way ANOVA with Dunnett's post hoc test to correct for multiple comparisons to vector (**H**). **C**: $F_{3,20}$ = 702.6. **D**: $F_{2,28}$ = 92.92. **E**: $F_{3,20}$ = 136. **F**: $F_{3,28}$ = 111.7. **G**: t = 5.86. **H**: $F_{2,21}$ = 49.87. Graphs are the mean ± SEM and depict 1 experiment that was replicated with similar results.

was measured before or up to 4 weeks after SNI surgery between WT and *BARP*-KOs (0.250 ± 0.066 g, 0.166 ± 0.043 g, respectively; Figure 6, F and G). Systemic nicotine administration exerts antiallodynia in rodent models of neuropathic pain (8, 32). Fitting with this, we found that intraperitoneal (i.p.) administration of nicotine (1.0 mg/kg) reduced mechanical allodynia following nerve injury in WT animals (Figure 6F). However, nicotine had no such relieving effect in *BARP*-KO mice (WT, 0.529 ± 0.101 g; *BARP*-KO, 0.248 ± 0.064 g; Figure 6F).

We next asked whether the antiallodynic deficits observed in *BARP*-KO mice were specific to α6β4. NACHO is an essential chaperone for brain α7 receptors and promotes assembly of other nAChRs such as α4β2, α3β2, and α6β2β3 (11). Further, NACHO knockouts show dramatically reduced brain epibatidine binding (12) and striatal α-CTXMII binding (12). Importantly, we show here that α6β4 occupies a privileged role compared with other nAChR subtypes, as NACHO has no effect on α6β4 function (Supplemental Figure 1, A and E; Supplemental Figure 2, A and B).
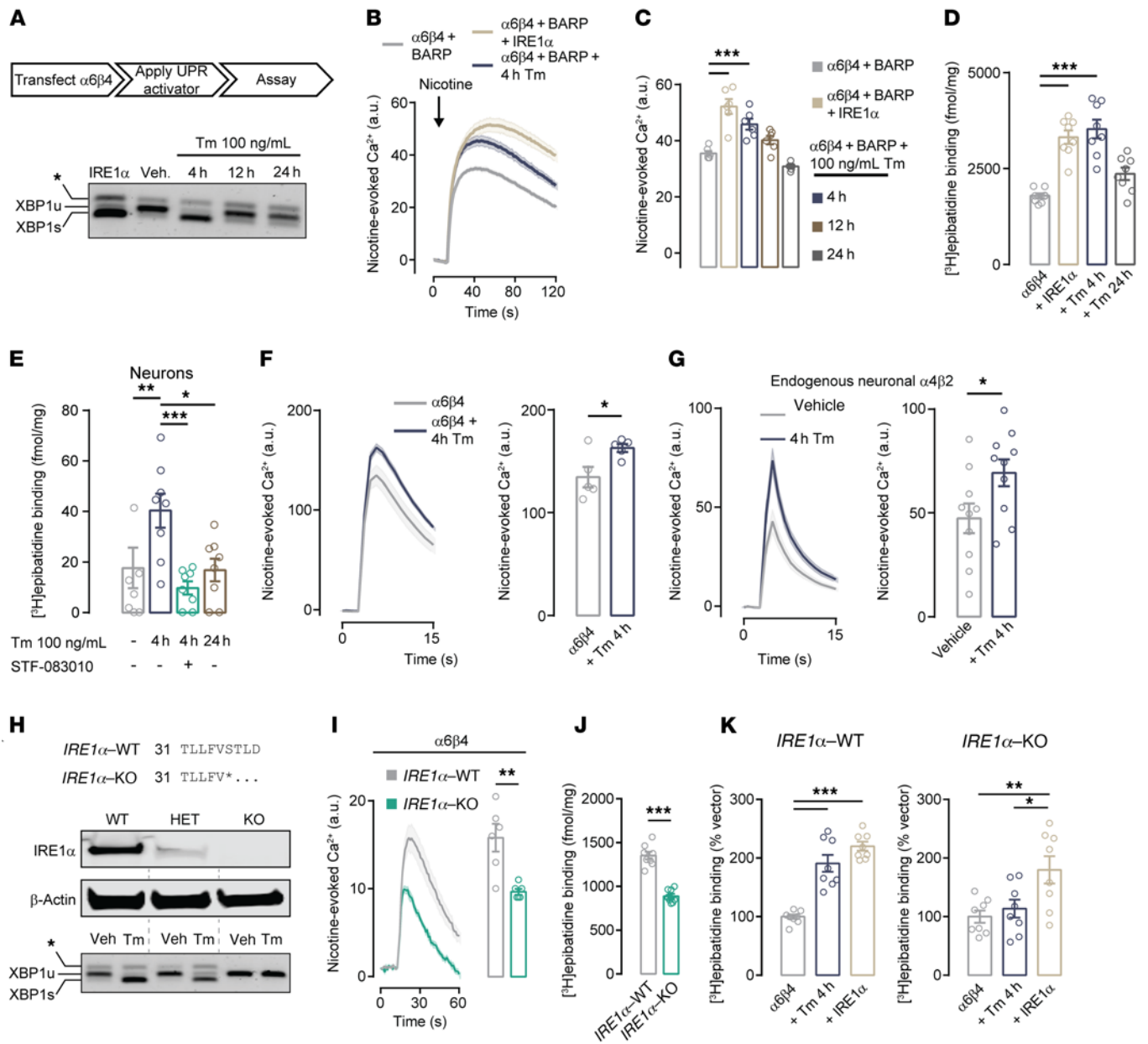
Figure 5. Endogenous IRE1α enhances α6β4 assembly. (A) HEK293T cells were transfected with α6β4 and treated with tunicamycin (Tm, 100 ng/mL) as indicated. Tm induced splicing of XBP1 (XBP1s) at 4 hours. XBP1u, unspliced XBP1. **(B and C)** Tm treatment for 4, but not 12 or 24 hours enhanced nicotine-induced (7.5 μM) α6β4 FLIPR responses. $n = 6$ for each condition except $n = 5$ for BARP + IRE1α. **(D)** [³H]epibatidine binding to α6β4 in HEK293T cells with indicated treatments. $n = 8$ each. **(E)** [³H]epibatidine binding to cortical neuron lysates transduced with α6β4. IRE1α inhibitor STF-083010 (20 μM) applied 30 minutes before Tm (100 ng/mL). $n = 8$ each. **(F)** Nicotine-evoked (50 μM) Ca²⁺ responses in cortical neurons transduced with α6β4 lentiviral particles. $n = 5$ for each condition. **(G)** Endogenous α4β2-mediated Ca²⁺ responses in cortical neurons. $n = 10$ for each condition. **(H)** Top: CRISPR/Cas9-mediated strategy for stop codon (*) insertion in IRE1α. Middle: Immunoblotting confirmed IRE1α protein knockout. Bottom: IRE1α activity in IRE1α-heterozygous (IRE1α-HET) and IRE1α-knockout (IRE1α-KO) lines. RT-PCR shows that the KO line lacks XBP1 splicing activity. **(I)** Nicotine-evoked (100 μM) FLIPR traces (left) and quantification (right) from IRE1α-WT and IRE1α-KO HEK293T cell lines transfected with α6β4 and BARP. $n = 6$ for each condition. **(J)** [³H]epibatidine binding in IRE1α-WT and IRE1α-KO cells transfected with α6β4. $n = 8$ each. **(K)** [³H]epibatidine binding to cells transfected with α6β4. Tm treatment increased binding in WT, but not IRE1α-KO cells, and cotransfection with IRE1α increased binding in both lines. $n = 8$ each. *$P < 0.05$; **$P < 0.01$; ***$P < 0.001$ by 1-way ANOVA with Dunnett's post hoc test compared with α6β4 alone (**C** and **D**), unpaired t test (**F–J**), or 1-way ANOVA with Tukey's post hoc test (**E** and **K**). **C**: $F_{4,25} = 24.92$. **D**: $F_{3,28} = 22.29$. **E**: $F_{3,27} = 8.115$. **K**: $F_{2,21} = 41.93$ for IRE1α-WT, $F_{2,21} = 6.197$ for IRE1α-KO. Graphs are the mean ± SEM and depict 1 experiment that was replicated with similar results.

To this end, we performed SNI surgery on *NACHO*-KO mice and tested mechanical allodynia. No difference in mechanical allodynia was observed after SNI surgery (Supplemental Figure 7F). Furthermore, *NACHO*-KO mice exhibited significant nicotine-induced antiallodynia at levels comparable to WT (gram threshold levels WT, 0.854 ± 0.217 g; *NACHO*-KO, 0.566 ± 0.118 g), indicating that the deficits seen in *BARP*-KO mice were predominantly mediated via α6β4 (Supplemental Figure 7, F and G).
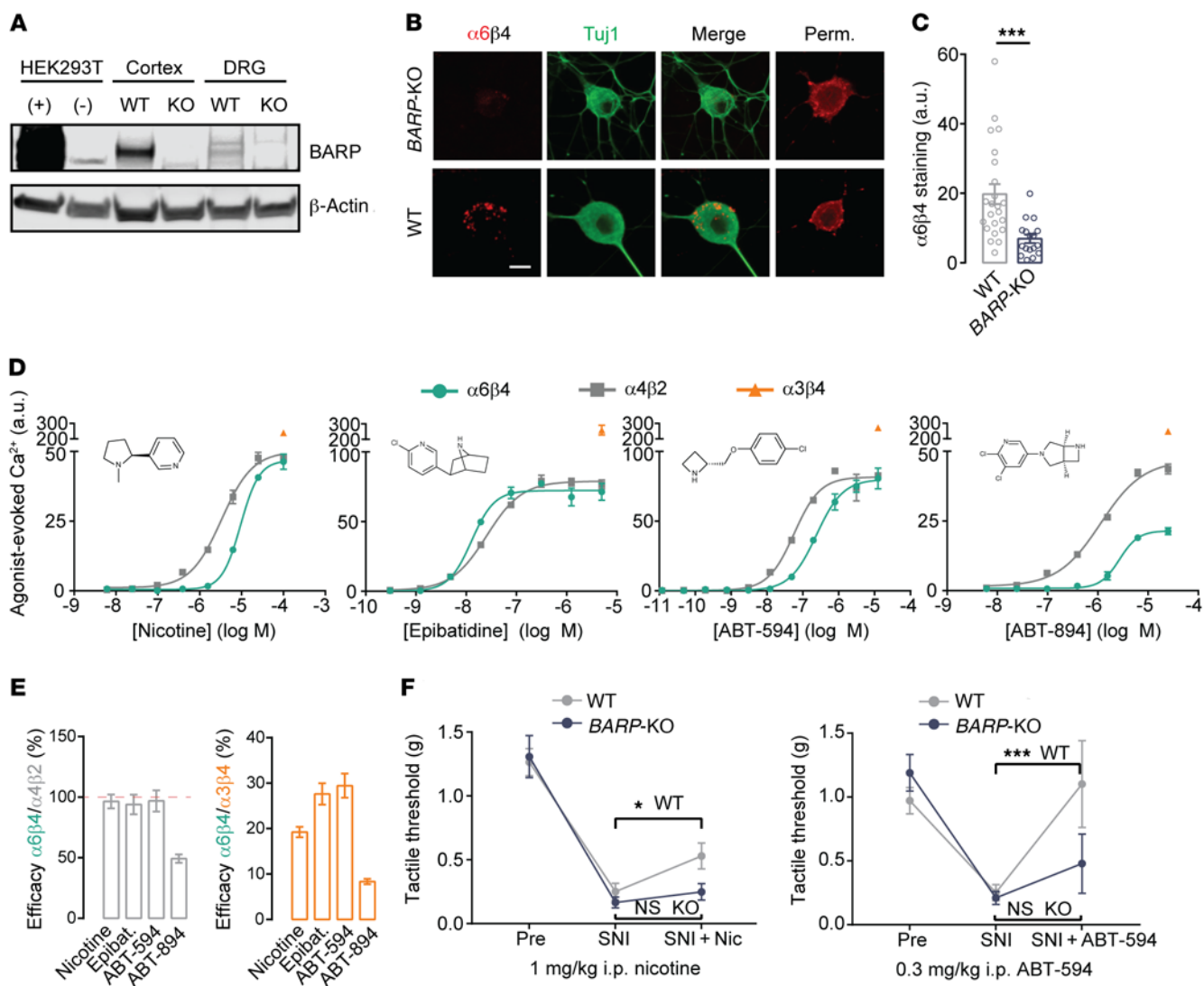
Figure 6. BARP promotes α6β4 function in vivo and mediates antiallodynia. (**A**) Immunoblotting identified BARP protein in cerebral cortex and dorsal root ganglia (DRG) from WT but not *BARP*-KO mice. BARP-transfected HEK293T cells and β-actin served as controls. (**B** and **C**) Imaging (**B**) and quantification (**C**) of surface α6 in DRG neurons from WT and *BARP*-KO mice. Neurons were transduced with lentivirus expressing α6-V5 and β4 subunits and were stained with anti-V5 antibody. Surface staining for α6 is reduced in *BARP*-KO neurons, whereas permeabilized (Perm) neurons show similar total levels of receptor. Scale bar: 10 μm. *n* = 23 and 17 neurons for WT and *BARP*-KO, respectively. (**D**) FLIPR responses in transfected HEK293T cells stimulated with indicated compounds. Cells transfected with α6β4 were cotransfected with BARP, IRE1α, and SULT2B1 (for values see Supplemental Tables 1 and 2). Shown are concentration-response curves for α6β4 and α4β2 and a single high concentration for α3β4. (**E**) Quantification of maximal compound efficacy on α6β4 vs. α4β2 (left) or α3β4 (right). (**F** and **G**) Mechanical allodynia was assessed in WT and *BARP*-KO mice before (Pre) and following spared nerve injury (SNI) surgery. WT, but not *BARP*-KO mice exhibited significant (**F**) nicotine-mediated and (**G**) ABT-594–mediated antiallodynia. *n* = 10 and 12 for WT and *BARP*-KO, respectively in **F**. *n* = 11 for each group for **G**. *$P < 0.05$; ***$P < 0.001$ by Mann-Whitney test (**C**) or linear mixed-effects model for repeated measures comparing SNI-baseline to SNI-treatment time point (**F** and **G**). **C**: $U = 57$. **F**: $P = 0.05$ for WT, SNI vs. SNI + nicotine; $P = 0.35$ for *BARP*-KO. **G**: $P < 0.001$ for WT, SNI vs. SNI + nicotine; $P = 0.4$ for *BARP*-KO. Graphs are the mean ± SEM. Graphs in **C**–**E** are representative of 1 experiment and were replicated with similar results.

To provide further pharmacological evidence of non–α4β2-mediated antiallodynia in SNI, we pretreated WT animals with a potent α4β2 antagonist, dihydro-β-erythroidine (DHβE), at a dose previously shown to block central effects of systemically administered nicotine (33, 34). After allodynia induction via SNI surgery, animals were injected subcutaneously with 1 mg/kg DHβE 20 minutes before nicotine administration and tested for paw withdrawal thresholds (35). Animals pretreated with DHβE and saline both exhibited robust nicotine-induced

antiallodynia (Supplemental Figure 7H; saline, 0.630 ± 0.171 g; DHβE, 0.702 ± 0.131 g).

Finally, to understand whether the clinical efficacy of ABT-594 may be mediated by α6β4, we injected a separate cohort of *BARP*-KO mice with ABT-594 (0.3 mg/kg; i.p.). Importantly, ABT-594 alleviated mechanical allodynia in WT but not *BARP*-KO animals (Figure 6G), further supporting our model that BARP is crucial for α6β4 function and nicotinic agent–induced antiallodynia (WT SNI, 0.252 ± 0.062 g; WT SNI + ABT-594, 1.102 ± 0.341 g; *BARP*-KO

SNI, 0.210 ± 0.051 g; *BARP*-KO SNI + ABT-594, 0.479 ± 0.232 g). Whereas previous studies found that the nonspecific nicotinic antagonist mecamylamine blocks ABT-594's antiallodynic effect (36), animals pretreated with DHβE retained significant ABT-594 antiallodynia (Supplemental Figure 7I; saline, 2.568 ± 0.422 g; DHβE, 2.059 ± 0.292 g), highlighting a non-α4β2 mechanism.

Discussion

The cholinergic system participates in numerous neurodegenerative and neuropsychiatric disorders. However, many nAChRs cannot be functionally expressed, which has impeded drug discovery. Genome-wide cDNA screening here identified accessory proteins required for activity of the previously intractable α6β4 receptor and unlock future high-throughput screening efforts. These findings expand the array of partner proteins that differentially control nAChRs. Whereas NACHO regulates most nAChRs, NACHO has no effect on α6β4. The α6-containing nAChRs themselves show selectivity, as NACHO, BARP, SULT2B1, and LAMP5 affect α6β2β3 (13), whereas α6β4 is regulated by BARP, IRE1α, and SULT2B1. These multiple layers of molecular control may allow precise regulation of nAChRs during specific developmental and physiological circumstances. Accordingly, α6β2β3 concentrates at presynaptic terminals of certain monoaminergic neurons, and this may be enabled by the lysosomal protein LAMP5, which displays a similar restricted distribution (37). On the other hand, LAMP5 is absent from DRG and does not regulate α6β4.

IRE1α promotes α6β4 assembly via the UPR pathway. Previous studies in *C. elegans* identified a component of the ER membrane complex as critical for nAChR assembly and function (38). In mammals, nicotine-induced upregulation of nAChRs reduces the UPR including IRE1α, suggesting an important interplay (39, 40). Furthermore, a recent report identified a direct chaperone role for IRE1α on IP$_3$ receptors at mitochondria-associated membranes that did not require its kinase or RNase activities (41). In contrast, effects on α6β4 require IRE1α's canonical kinase and RNase functions. Several observations suggest that this new IRE1α role on nAChRs is physiologically relevant. First, IRE1α enhanced responses from a subset of nAChR combinations, but IRE1α did not affect other channels. Second, ATF6 and PERK, 2 other arms of the UPR, failed to enhance assembly of nAChRs, suggesting that IRE1α's effects are not a generalized consequence of UPR activation. Third, knockout of endogenous IRE1α decreased α6β4 binding and function. Finally, activating endogenous IRE1α with Tm enhanced function of exogenous α6β4 and endogenous α4β2 in neurons.

Promotion of α6β4 assembly by IRE1α fits conceptually with the latter's role as a sensor of the UPR, which promotes protein folding in the ER during cell stress (16). Indeed, effects on α6β4 involve the canonical IRE1α pathway of autophosphorylation and splicing to form XBP1s. Once spliced, XBP1s translocates to the nucleus and upregulates chaperones such as Erdj4 and calnexin, which improves ER protein folding capacity (42–44). Accordingly, calnexin directly enhances assembly of muscle-type nAChRs (45). Precisely how XBP1s promotes α6β4 assembly requires further study.

BARP promotes function of multiple nAChRs. BARP's robust enhancement of α6β4 function in HEK cells, oocytes, and neurons complements previous studies showing that BARP promotes

function of α6β2β3 and α3β2 receptors (13). Whereas BARP regulates gating of α6β2β3 and α3β2 channels (13), it instead increases surface trafficking of α6β4. Thus, BARP enhances multiple α6-containing nAChRs via distinct mechanisms. Yeast 2-hybrid screening originally identified BARP as a negative regulator of VGCCs. These studies found that 2 intracellular domains toward the BARP C-terminus bind to calcium channel β subunits (14). However, the calcium channel–binding domains of BARP are not involved in regulation of α6β4. Instead, we find that a more membrane-proximal region between BARP amino acids 101 and 202 regulates α6β4. This suggests that BARP may function as a scaffold linking certain nAChRs with calcium channels. Such a model fits with experiments showing that cholinergic regulation of neurotransmitter release often involves calcium channel opening downstream of nAChRs (46, 47).

Targeting α6β4 receptors to treat neuropathic pain. Functional reconstitution of α6β4 receptors has important implications for neuropharmacology. Nicotine has long been recognized as an analgesic (48). Epibatidine is 200 times more potent than morphine in blocking nociception (49), but its side effects preclude clinical development (36). As several nAChR subtypes are expressed in DRG sensory neurons, and epibatidine is a pan-nicotinic agonist, the molecular target for its analgesia remains uncertain. α4β2 nAChRs have been classically thought to mediate nAChR-induced analgesia, yet years of research have yielded no approved therapeutics, suggesting involvement of a different receptor subtype (7). Recently, a genomics screen of DRG tissue from 25 inbred mouse strains identified the α6 nAChR subunit as the major phenotypic contributor to allodynia (8). Furthermore, knockout mouse studies showed that α6 but not α4 is required for peripheral and spinal nicotine-induced analgesia (8). The precise mechanisms through which nicotinic agents mediate analgesia are uncertain. Previous work suggested that α6β4 can produce analgesia via cross-inhibition of P2X2/3 receptors on DRG neurons (8, 50). Activation of nAChRs may also promote analgesia via blunting of TrpV1-mediated currents in DRG nociceptors (51).

Here, we find that *BARP*-KO mice, which have impaired α6β4 surface expression in DRG, lack nicotine-mediated antiallodynia. Because BARP also promotes α3β2 and α6β2β3 function, we leveraged the fact that NACHO has no effect on α6β4 but promotes α3β2 and α6β2β3 assembly. We observed normal nicotine-induced allodynia in *NACHO*-KO mice, suggesting that the deficits observed in *BARP*-KO mice are mediated predominantly via α6β4 and not other nAChR subtypes. Supporting this, *BARP* KO did not alter surface expression of other nAChRs in DRG.

Phase II clinical studies found that ABT-594, a nicotinic agent related to epibatidine, was effective in treating diabetic neuropathic pain but had unacceptable side effects (29). The investigators hypothesized that activity at α4β2 was mediating analgesia, while α3β4 was predominantly responsible for the untoward side effects. As such, maximizing activity at α4β2 while minimizing α3β4 activity drove development of the follow-up compound, ABT-894. Unfortunately, ABT-894 was clinically ineffective (30). The study investigators hypothesized that "it is possible that ABT-594, which is a less selective α4β2 [neuronal nicotinic receptor (NNR)] agonist than ABT-894, elicits some of its effects via activity at non-α4β2 NNRs. If this is the case, the preferential affinity

of ABT-894 for α4β2 NNRs may have been a disadvantage that resulted in a lack of analgesic efficacy" (30). Thus, the pharmacological difference between ABT-594 and -894 that accounts for their discrepant clinical efficacy is uncertain and likely involves non-α4β2 nAChRs.

Our ability to express functional α6β4 receptors showed that ABT-594 exhibits similar efficacy on α4β2 and α6β4. In contrast, ABT-894 exhibited only weak partial agonism on α6β4 as compared with α4β2 (Figure 6, D and E; Supplemental Table 1). We further show that the effective analgesics nicotine and epibatidine exhibit similar efficacies on α4β2 and α6β4. This unexpected pharmacology of α6β4 provides a likely explanation for the differential clinical efficacy of ABT-594 versus ABT-894. That is, α6β4 activity contributed to ABT-594's clinical analgesia, yet ABT-894's diminished α6β4 efficacy may underpin the lack of its clinical efficacy. Supporting this model, ABT-594 exerts antiallodynic effects in WT mice but has no effect in *BARP*-KO mice, whose DRG have reduced α6β4 surface expression. Furthermore, pretreatment with the potent α4β2 antagonist DHβE failed to block ABT-594–induced antiallodynia, further supporting a non-α4β2 mechanism for alleviating neuropathic pain in the SNI model. ABT-594 alleviates thermal and inflammatory pain, suggesting that α6β4 agonists may be useful for a broad spectrum of pain conditions (36).

Methods

Cell culture and transfection. Expression plasmids for the following genes were used in this study (all human, GenBank accession numbers): *CHRNA6* (NM_004198), *CHRNA4* (NM_000744.6), *CHRNA3* (NM_000743.5), *CHRNA7* (NM_000746.5), *CHRNB2* (NM_000748.2), *CHRNB3* (NM_000749.5), *CHRNB4* (NM_000750), *BARP* (XM_017026555), *ERN1* (IRE1α), *PERK* (NM_001313915.1), *ATF6* (NM_007348.4), *NACHO* (NM_021637.2), *SULT2B1* (NM_177973), *LAMP5* (NM_012261.4), *5HT3A* (NM_213621.4), *GLUA1* (NM_000827.4), *GABBR1* (NM_021903.2), and *GABBR2* (NM_005458.8).

HEK293T cells were initially purchased from ATCC and cultured in DMEM high-glucose medium supplemented with 10% FBS and 1 mM sodium pyruvate. Cells were transfected at 80%–90% confluence more than 4 hours after plating with FuGENE 6 or ViaFect Transfection Reagent (Promega) and incubated at 37°C. To promote surface expression, cells were switched to 30°C after 24 hours. All assays unless otherwise noted were performed 48–72 hours after transfection. For cDNA library screening, expression-ready cDNA plasmids from a Broad Institute library were cotransfected in 384-well plates with α6β4 subunits in a 1:1:1 ratio.

For neuronal FLIPR and epibatidine experiments, rat cortical E18 neurons were purchased from BrainBits, dissociated with papain, and cultured in NbActiv media (BrainBits) at 37°C. Cultures were transduced with lentiviral particles expressing α6 and β4 (Vigene Biosciences) at DIV 7 and assayed at DIV 13. Cultures were pretreated with compounds for indicated time periods before assay.

For DRG neuron staining, DRGs from adult WT or *BARP*−/− mice were dissected in cold L-15 media supplemented with GlutaMAX (Thermo Fisher Scientific). DRGs were dissociated with collagenase/protease IV solution for 60 minutes. DRGs were triturated with a fire-polished glass pipette, resuspended in L-15 media, and filtered with a cell strainer. Cells were then pipetted on top of a 60%/30% Percoll

gradient and centrifuged at 800*g* for 20 minutes at 4°C. After centrifugation, the top layer was discarded, and neurons were collected and spun down at 200*g* for 10 minutes. The supernatant was aspirated, and cells were resuspended in Neurobasal A supplemented with B-27, GlutaMAX, and 25 ng/mL nerve growth factor. Neurons were then plated on glass coverslips coated with poly-D-lysine (PDL) and laminin. Cells were transduced 1 hour after plating and assayed 5 days later.

SNI and tactile threshold testing. For the SNI procedure, adult male mice (23–33 g) were deeply anesthetized with isoflurane and SNI surgery was performed as described previously (31). Briefly, the sural and common peroneal branches of the left sciatic nerve were ligated, leaving the tibial branch intact. Only mice that did not exhibit motor dysfunction (e.g., paw dragging) were used.

For tactile threshold testing, following a 30-minute acclimation on the von Frey stand, preinjury tactile thresholds were measured from the left hind paw and recorded before SNI surgery. Fifty-percent tactile paw withdrawal thresholds (PWTs) were measured from the left paw and recorded using calibrated von Frey filaments applied perpendicularly with sufficient force to bend slightly and held for 2–3 seconds against the plantar surface. Paw flinching during or immediately following removal of the stimulus was scored as positive. PWT was tested at preinjury levels and at 1, 3, 7, 14, and 21 days (21 days deemed SNI) following surgery. At 29 days following surgery, mice were i.p. injected with vehicle, 1.0 mg/kg (–)-nicotine (Millipore-Sigma), or 0.3 mg/kg ABT-594 (Tocris) and again tested at either 10 minutes (nicotine) or 1 hour (ABT-594) after injection. For DHβE pretreatment experiments, DHβE was dissolved in saline and administered subcutaneously at a final concentration of 1 mg/kg 20 minutes before nicotine or ABT-594 injection. Experimenters were blinded to genotype throughout the study.

Molecular biology. IRE1α mutants (K907A, RNAmut; K599A, KINmut; I642G, CONDmut) were generated via site-directed mutagenesis and confirmed by sequencing. BARP101 and BAPR202 truncation mutants were generated by inserting a premature stop codon at amino acid 102 and 203, respectively.

The α4N/6 chimera consisted of the first 242 amino acids corresponding to the N-terminal extracellular region of α4 fused to the transmembrane and intracellular regions of α6 (amino acids 240–495). Conversely, the α6N/4 chimera consisted of the first 239 amino acids of α6 fused to the transmembrane and intracellular regions of α4 (amino acids 243–628). Loop chimeras substituted amino acids 331–600 for α4 and 328–465 for α6. All chimeras were confirmed by sequencing.

To generate *IRE1α*-KO cell lines, a guide RNA targeting exon 2 of the IRE1α gene was cotransfected into HEK293T cells with Cas9 enzyme (IDT Technologies) and single-stranded oligodeoxynucleotide (ssODN) for homology-directed repair using TransIT-X2 transfection reagent (Mirus, MIR6003). Serine at position 36 was mutated to a stop codon. Single clones were isolated, expanded, sequenced, and confirmed for hetero- or homozygosity with a Zero Blunt TOPO PCR Cloning Kit (Thermo Fisher Scientific, K280020SC). ssODN sequence: CAGATTTTTGGAAGTACCAGCACAGTGACGCTTCCT-GAAACCTTGTTGTTTGTGTAAACGCTGGATGGAAGTTTGCAT-GCTGTCAGCAAGAGGACAGGCTCAATCAAATGG.

For XBP1s RT-PCR experiments, HEK293T cells were seeded in 6-well plates and treated with vehicle or Tm for the indicated time points. Cells were then collected and RNA isolated using an RNeasy Mini Kit (QIAGEN, 74104). cDNA was synthesized from total RNA

with a SuperScript IV First-Strand Synthesis System (Thermo Fisher Scientific, 18091050) according to the manufacturer's instructions. The following primers were used to amplify *XBP1* cDNA with PCR (25): XBP1sense, TTACGAGAGAGAAAACTCATGGC; antisense, GGGTCCAAGTTGTCCAGAATGC.

FLIPR assays. HEK293T cells were seeded at 15,000/well in 384-well glass-bottomed PDL-coated plates (Corning). At the time of assay, cells were washed once with FLIPR buffer (HyClone HEPES-buffered saline [GE Life Sciences] with [in mM] 149 NaCl, 4 KCl, 10 HEPES, 5 glucose, 2 $CaCl_2$, 1 $MgCl_2$; 300 mOsm and pH 7.4) and loaded for 1 hour at room temperature with Calcium5 dye (Molecular Devices). After dye loading, excess dye was removed, plates were washed once with FLIPR buffer, and then placed in a FLIPR Tetra (Molecular Devices) machine. Compound-induced Ca^{2+} responses were monitored and measured for 5 minutes with Screenworks software (Molecular Devices). For α6β2β3* responses, α6/3 chimera and β3 mutant were used to enable larger responses (13). For α7 responses, cells were first incubated with the positive allosteric modulator PNU-120596 (5 μM). Unless otherwise noted, all FLIPR transfections were carried out at a 3:1:5 ratio (α6/β4/chaperone). XBP1s transfections were carried out at a ratio of 3:1:0.1 (α6/β4/XBP1s). For neuronal assays, the FLIPR protocol was identical except that 3 mM $CaCl_2$ was used in FLIPR buffer. To isolate α6β4 responses from endogenously expressed α4β2, neurons were incubated for 5 minutes with 25 μM DHβE before stimulation with nicotine.

Immunofluorescent surface staining. HEK293T cells were seeded at 10,000/well in 384-well glass-bottomed PDL-coated plates (Corning). All cell transfections included EGFP to label cytoplasm of transfected cells. For staining, cells were incubated for 1 hour with fluorescent-conjugated antibody against HA or V5 tag (Dylight HA-650 [26183-D650], Alexa Fluor V5-555 [37-7500-A555], Invitrogen) at 30°C. Cells were washed with PBS and then fixed for 45 minutes ar room temperwature with 4% paraformaldehyde. After washing, nuclei were stained with NucBlue solution (Invitrogen). Plates were imaged using the Opera Phenix confocal instrument (PerkinElmer) at ×20 magnification. For image analysis, Columbus automated software was used (PerkinElmer). Briefly, EGFP labeling was used for automatic cell detection. Then, average fluorescence intensity was measured in a ring region surrounding the cell, but not including the cytoplasm, which represented surface staining.

For DRG neuron staining, cells were live stained with the same anti-V5 primary antibody as described above. Cells were additionally costained with β-3 tubulin (Tuj1) conjugated to Alexa Fluor 488 (eBioscience, 53-4510-82) to label cell bodies and processes. For cytoplasmic staining, cells were fixed then permeabilized for 20 minutes at room temperature with 0.3% Triton X-100 in PBS. Neurons were imaged at ×40 magnification with a confocal microscope (Zeiss).

[³H]epibatidine binding. HEK293T cells or rat cortical E18 neurons were collected with PBS, spun down, and then resuspended in 50 mM ice-cold Trizma buffer (MilliporeSigma). Cells were homogenized for 30 seconds at max speed with a T-25 Ultra-Turrax homogenizer (Ika) and concentrations measured using the Pierce BCA assay (Thermo Fisher Scientific). Samples were run in 16 replicates and incubated with 10 nM [³H]epibatidine (PerkinElmer) for 2–3 hours at room temperature. In half of the samples, 10 μM unlabeled epibatidine (Tocris) was coapplied to determine nonspecific binding. Samples were filtered and bound to polyethylenimine-treated 96-well GF/B filter plates (PerkinElmer). Plates were washed with cold Trizma buffer and then desiccated for 20 minutes at 65°C. Each well received 60 μL of MicroScient-0, and then plates were read with a TopCount NXT scintillation counter (PerkinElmer).

Protein biochemistry. For immunoblotting, cells were collected into RIPA buffer (Thermo Fisher Scientific) with Halt protease and phosphatase inhibitor cocktail (Thermo Fisher Scientific). Cells were sonicated, spun down at 14,000*g* for 30 minutes at 4°C, and the supernatant was taken for further analysis. Protein concentrations were measured using the Pierce BCA assay. Protein lysates were denatured at 55°C for 30 minutes, proteins were resolved by SDS-PAGE, and blots were incubated overnight at 4°C with primary antibodies (anti–β-actin, Thermo Fisher Scientific [PA516914]; anti-IRE1α, Cell Signaling Technology [3294S]; anti-HA, Thermo Fisher Scientific [26183]; anti-V5, Thermo Fisher Scientific [PA1993]; and anti-BARP [ref. 13]). Blots were then incubated for 1 hour at room temperature in the dark with infrared-conjugated secondary antibodies and imaged using the Odyssey system (Licor).

For coimmunoprecipitation, cells were solubilized 2 hours at 4°C on a shaker in buffer containing 100 mM NaCl, 1% *n*-dodecyl-ᴅ-maltoside, and 1 mM iodoacetamide. Samples were spun at 20,000*g* at 4°C for 45 minutes. These lysates were incubated with 3 μg of immunoprecipitation antibody on a shaker overnight at 4°C. Protein-antibody complexes were captured with Protein A Dynabeads (Thermo Fisher Scientific). After washing, bound proteins were eluted by heating to 55°C for 30 minutes and were analyzed by immunoblotting.

Oocyte recordings. cRNAs were obtained via in vitro transcription with an mMessage mMACHINE T7 Transcription Kit (Thermo Fisher Scientific, AM1344). Stage 4/5 oocytes were purchased from EcoCyte Biosciences and injected with 60 ng total cRNA at a ratio of 1:1:2 α6/β4/chaperone. After injection, oocytes were placed in Modified Barth's Saline (MilliporeSigma) supplemented with gentamycin and incubated at 18°C. Recordings were made 3–5 days after cRNA injection and stimulated with 250 μM ACh for 2 seconds. Oocytes were recorded using the 2-electrode voltage-clamp method and held at –60 mV. Currents were acquired using a HEKA amplifier with FitMaster software (HEKA Elektronik). Data were sampled at 5 kHz and filtered with a 4-pole Bessel filter at 1 kHz.

Electrophysiology. HEK293T cells in 6-well plates were cotransfected with α6β4, chaperones, and EGFP, and 24 hours before recording were replated on 12-mm glass coverslips. For recordings, coverslips were placed in an extracellular bath composed of (in mM) 149 NaCl, 4 KCl, 10 HEPES, 5 glucose, 2 $CaCl_2$, and 1 $MgCl_2$. Borosilicate glass (World Precision Instruments) pipettes were pulled to obtain final resistances of 3–5 MΩ with a PC-10 micropipette puller (Narshige). Internal solution comprised (in mM) 145 CsCl, 2.5 NaCl, 10 HEPES, 4 MgATP, 1 EGTA; pH was adjusted to 7.4 with CsOH; osmolality was adjusted to 300 mOsm/kg with sucrose. After whole-cell recording from EGFP⁺ cells was achieved, cells were carefully lifted from the coverslip and moved toward a separate pipette with agonist. To record agonist-evoked responses, ACh was rapidly applied to cells held at –60 mV using a MXPZT piezoelectric actuator system (Siskiyou). Series resistances (3–15 MΩ) were compensated by at least 80%. All recordings were carried out with an Axopatch 200B amplifier (Molecular Devices). Signals were sampled at 25 kHz and low-pass filtered at 10 kHz. Data were acquired and analyzed

using pClamp10 software (Molecular Devices). Steady state/peak ratio was calculated as the amplitude of steady-state current during constant ACh application divided by the peak current.

Statistics. Results are represented as mean ± SEM unless otherwise noted. For data sets with 2 groups, an unpaired, 2-tailed Student's *t* test was used to test for significance. For 3 or more groups, 1-way ANOVA was used. To adjust for multiple comparisons: when comparing multiple groups to a control group, Dunnett's post hoc test was used. If differences between all groups to each other were tested, then Tukey's post hoc test was used. Significance levels were set at *$P < 0.05$, **$P < 0.01$, ***$P < 0.001$ unless otherwise noted in figure legends. The D'Agostino and Pearson omnibus test with an α value of 0.05 was used to test for normality. EC_{50} values and concentration-response curves were calculated using a variable slope, 4-parameter nonlinear regression model: $y = \text{bottom} + (x^{\text{Hill slope}}) \times (\text{top} - \text{bottom})/(x^{\text{Hill slope}} + EC_{50}^{\text{Hill slope}})$. All statistics and graphing were carried out with Prism (GraphPad).

Study approval. *BARP*-KO and *NACHO*-KO mice were previously described (12, 13). All procedures were performed in accordance with Janssen (La Jolla) IACUC guidelines.

1. Role LW, Berg DK. Nicotinic receptors in the development and modulation of CNS synapses. *Neuron*. 1996;16(6):1077–1085.
2. Gotti C, Clementi F. Neuronal nicotinic receptors: from structure to pathology. *Prog Neurobiol*. 2004;74(6):363–396.
3. Lindstrom J. Nicotinic acetylcholine receptors in health and disease. *Mol Neurobiol*. 1997;15(2):193–222.
4. Hogg RC, Raggenbass M, Bertrand D. Nicotinic acetylcholine receptors: from structure to brain function. *Rev Physiol Biochem Pharmacol*. 2003;147:1–46.
5. Le Novère N, Corringer PJ, Changeux JP. The diversity of subunit composition in nAChRs: evolutionary origins, physiologic and pharmacologic consequences. *J Neurobiol*. 2002;53(4):447–456.
6. Picciotto MR. Nicotine as a modulator of behavior: beyond the inverted U. *Trends Pharmacol Sci*. 2003;24(9):493–499.
7. Hone AJ, McIntosh JM. Nicotinic acetylcholine receptors in neuropathic and inflammatory pain. *FEBS Lett*. 2018;592(7):1045–1062.
8. Wieskopf JS, et al. The nicotinic α6 subunit gene determines variability in chronic pain sensitivity via cross-inhibition of P2X2/3 receptors. *Sci Transl Med*. 2015;7(287):287ra72.
9. Wang J, Kuryatov A, Lindstrom J. Expression of cloned α6* nicotinic acetylcholine receptors. *Neuropharmacology*. 2015;96(pt B):194–204.
10. Letchworth SR, Whiteaker P. Progress and challenges in the study of α6-containing nicotinic acetylcholine receptors. *Biochem Pharmacol*. 2011;82(8):862–872.
11. Gu S, et al. Brain α7 nicotinic acetylcholine receptor assembly requires NACHO. *Neuron*. 2016;89(5):948–955.
12. Matta JA, et al. NACHO mediates nicotinic acetylcholine receptor function throughout the brain. *Cell Rep*. 2017;19(4):688–696.
13. Gu S, Matta JA, Davini WB, Dawe GB, Lord B, Bredt DS. α6-Containing nicotinic acetylcholine receptor reconstitution involves mechanisti-

cally distinct accessory components. *Cell Rep*. 2019;26(4):866–874.e3.
14. Béguin P, et al. BARP suppresses voltage-gated calcium channel activity and Ca²⁺-evoked exocytosis. *J Cell Biol*. 2014;205(2):233–249.
15. Chen Y, Brandizzi F. IRE1: ER stress sensor and cell fate executor. *Trends Cell Biol*. 2013;23(11):547–555.
16. Walter P, Ron D. The unfolded protein response: from stress pathway to homeostatic regulation. *Science*. 2011;334(6059):1081–1086.
17. Kuryatov A, Olale F, Cooper J, Choi C, Lindstrom J. Human alpha6 AChR subtypes: subunit composition, assembly, and pharmacological responses. *Neuropharmacology*. 2000;39(13):2570–2590.
18. Papke RL, et al. Extending the analysis of nicotinic receptor antagonists with the study of alpha6 nicotinic receptor subunit chimeras. *Neuropharmacology*. 2008;54(8):1189–1200.
19. Dash B, Bhakta M, Chang Y, Lukas RJ. Identification of N-terminal extracellular domain determinants in nicotinic acetylcholine receptor (nAChR) α6 subunits that influence effects of wild-type or mutant β3 subunits on function of α6β2*- or α6β4*-nAChR. *J Biol Chem*. 2011;286(44):37976–37989.
20. Kouvatsos N, Giastas P, Chroni-Tzartou D, Poulopoulou C, Tzartos SJ. Crystal structure of a human neuronal nAChR extracellular domain in pentameric assembly: Ligand-bound α2 homopentamer. *Proc Natl Acad Sci U S A*. 2016;113(34):9635–9640.
21. Han D, et al. IRE1alpha kinase activation modes control alternate endoribonuclease outputs to determine divergent cell fates. *Cell*. 2009;138(3):562–575.
22. Maly DJ, Papa FR. Druggable sensors of the unfolded protein response. *Nat Chem Biol*. 2014;10(11):892–901.
23. Papa FR, Zhang C, Shokat K, Walter P. Bypassing a kinase activity with an ATP-competitive drug. *Science*. 2003;302(5650):1533–1537.
24. Jiang H, et al. Unfolded protein response induc-

ers tunicamycin and dithiothreitol promote myeloma cell differentiation mediated by XBP-1. *Clin Exp Med*. 2015;15(1):85–96.
25. Lin JH, et al. IRE1 signaling affects cell fate during the unfolded protein response. *Science*. 2007;318(5852):944–949.
26. Ray P, et al. Comparative transcriptome profiling of the human and mouse dorsal root ganglia: an RNA-seq-based resource for pain and sensory neuroscience research. *Pain*. 2018;159(7):1325–1345.
27. Hone AJ, Meyer EL, McIntyre M, McIntosh JM. Nicotinic acetylcholine receptors in dorsal root ganglion neurons include the α6β4* subtype. *FASEB J*. 2012;26(2):917–926.
28. Moser N, et al. Evaluating the suitability of nicotinic acetylcholine receptor antibodies for standard immunodetection procedures. *J Neurochem*. 2007;102(2):479–492.
29. Rowbotham MC, Duan WR, Thomas J, Nothaft W, Backonja MM. A randomized, double-blind, placebo-controlled trial evaluating the efficacy and safety of ABT-594 in patients with diabetic peripheral neuropathic pain. *Pain*. 2009;146(3):245–252.
30. Rowbotham MC, et al. Efficacy and safety of the α4β2 neuronal nicotinic receptor agonist ABT-894 in patients with diabetic peripheral neuropathic pain. *Pain*. 2012;153(4):862–868.
31. Shields SD, Eckert WA, Basbaum AI. Spared nerve injury model of neuropathic pain in the mouse: a behavioral and anatomic analysis. *J Pain*. 2003;4(8):465–470.
32. Kyte SL, et al. Nicotine prevents and reverses paclitaxel-induced mechanical allodynia in a mouse model of CIPN. *J Pharmacol Exp Ther*. 2018;364(1):110–119.
33. Davis JA, Gould TJ. The effects of DHBE and MLA on nicotine-induced enhancement of contextual fear conditioning in C57BL/6 mice. *Psychopharmacology (Berl)*. 2006;184(3–4):345–352.
34. Li S, et al. Nicotine inhibits rapamycin-induced pain through activating mTORC1/S6K/IRS-1-related feedback inhibition loop. *Brain Res Bull*.

2019;149:75–85.

35. Damaj MI, Welch SP, Martin BR. In vivo pharmacological effects of dihydro-beta-erythroidine, a nicotinic antagonist, in mice. *Psychopharmacology (Berl)*. 1995;117(1):67–73.

36. Bannon AW, et al. Broad-spectrum, non-opioid analgesic activity by selective modulation of neuronal nicotinic acetylcholine receptors. *Science*. 1998;279(5347):77–81.

37. Tiveron MC, et al. LAMP5 fine-tunes GABAergic synaptic transmission in defined circuits of the mouse brain. *PLoS One*. 2016;11(6):e0157052.

38. Richard M, Boulin T, Robert VJ, Richmond JE, Bessereau JL. Biosynthesis of ionotropic acetylcholine receptors requires the evolutionarily conserved ER membrane complex. *Proc Natl Acad Sci U S A*. 2013;110(11):E1055–E1063.

39. Srinivasan R, et al. Pharmacological chaperoning of nicotinic acetylcholine receptors reduces the endoplasmic reticulum stress response. *Mol Pharmacol*. 2012;81(6):759–769.

40. Srinivasan R, et al. Smoking-relevant nicotine concentration attenuates the unfolded protein response in dopaminergic neurons. *J Neurosci*.

2016;36(1):65–79.

41. Carreras-Sureda A, et al. Non-canonical function of IRE1α determines mitochondria-associated endoplasmic reticulum composition to control calcium transfer and bioenergetics. *Nat Cell Biol*. 2019;21(6):755–767.

42. Lee AH, Iwakoshi NN, Glimcher LH. XBP-1 regulates a subset of endoplasmic reticulum resident chaperone genes in the unfolded protein response. *Mol Cell Biol*. 2003;23(21):7448–7459.

43. Rutkowski DT, et al. The role of p58IPK in protecting the stressed endoplasmic reticulum. *Mol Biol Cell*. 2007;18(9):3681–3691.

44. Shoulders MD, et al. Stress-independent activation of XBP1s and/or ATF6 reveals three functionally diverse ER proteostasis environments. *Cell Rep*. 2013;3(4):1279–1292.

45. Chang W, Gelman MS, Prives JM. Calnexin-dependent enhancement of nicotinic acetylcholine receptor assembly and surface expression. *J Biol Chem*. 1997;272(46):28925–28932.

46. McGehee DS, Heath MJ, Gelber S, Devay P, Role LW. Nicotine enhancement of fast excitatory synaptic transmission in CNS by presynaptic

receptors. *Science*. 1995;269(5231):1692–1696.

47. Kulak JM, McIntosh JM, Yoshikami D, Olivera BM. Nicotine-evoked transmitter release from synaptosomes: functional association of specific presynaptic acetylcholine receptors and voltage-gated calcium channels. *J Neurochem*. 2001;77(6):1581–1589.

48. Mattila MJ, Ahtee L, Saarnivaara L. The analgesic and sedative effects of nicotine in white mice, rabbits and golden hamsters. *Ann Med Exp Biol Fenn*. 1968;46(1):78–84.

49. Daly JW, Garraffo HM, Spande TF, Decker MW, Sullivan JP, Williams M. Alkaloids from frog skin: the discovery of epibatidine and the potential for developing novel non-opioid analgesics. *Nat Prod Rep*. 2000;17(2):131–135.

50. Limapichat W, Dougherty DA, Lester HA. Subtype-specific mechanisms for functional interaction between α6β4* nicotinic acetylcholine receptors and P2X receptors. *Mol Pharmacol*. 2014;86(3):263–274.

51. Fucile S, Sucapane A, Eusebi F. Ca²⁺ permeability of nicotinic acetylcholine receptors from rat dorsal root ganglion neurones. *J Physiol (Lond)*. 2005;565(pt 1):219–228.